A Statistical Study on the Frequency-dependent Damping of the Slow-mode Waves in Polar Plumes and Interplumes

Sudip Mandal[1] , S. Krishna Prasad[1,3] , and Dipankar Banerjee[1,2]
[1] Indian Institute of Astrophysics, Koramangala, Bangalore 560034, India; sudip@iiap.res.in
[2] Center of Excellence in Space Sciences India, IISER Kolkata, Mohanpur 741246, West Bengal, India

Abstract

We perform a statistical study on the frequency-dependent damping of slow waves propagating along polar plumes and interplumes in the solar corona. Analysis of a large sample of extreme ultraviolet imaging data with high spatial and temporal resolutions obtained from Atmospheric Imaging Assembly (AIA)/*Solar Dynamics Observatory* suggests an inverse power-law dependence of the damping length on the periodicity of slow waves (i.e., the shorter-period oscillations exhibit longer damping lengths), in agreement with the previous case studies. Similar behavior is observed in both plume and interplume regions studied in AIA 171 Å and AIA 193 Å passbands. It is found that the short-period (2–6 minutes) waves are relatively more abundant than their long-period (7–30 minutes) counterparts, in contrast to the general belief that the polar regions are dominated by the longer-period slow waves. We also derived the slope of the power spectra (α, the power-law index) statistically to better understand the characteristics of turbulence present in the region. It is found that the α values and their distributions are similar in both plume and interplume structures across the two AIA passbands. At the same time, the spread of these distributions also indicates the complexity of the underlying turbulence mechanism.

Key words: Sun: corona – Sun: magnetic fields – Sun: oscillations – Sun: UV radiation

1. Introduction

Slow magnetoacoustic waves (or simply, slow waves) are compressible magnetohydrodynamic (MHD) waves, which typically propagate along the magnetic field lines in solar corona (Roberts 2000). These waves are found in a variety of structures across different layers of the solar atmosphere (Banerjee et al. 2007). However, in this paper, we are only interested in the coronal counterpart of these waves as seen in large-scale coronal structures such as polar plumes (Banerjee & Krishna Prasad 2016). Polar plumes are the long and thin "ray"-like structures which trace open magnetic field lines emerging from the unipolar coronal hole regions (Poletto 2015). One of the first detections of slow waves was reported by DeForest & Gurman (1998) who used extreme ultraviolet (EUV) imaging data to show propagating intensity disturbances (later interpreted as slow waves) along polar plumes. These waves are ubiquitous in the solar corona (Krishna Prasad et al. 2012) with their apparent speeds ranging from 50 to 150 km s^{-1} (Kiddie et al. 2012). Such omnipresent nature, along with easy detectability, often makes these slow waves an important tool for coronal seismology (King et al. 2003; Van Doorsselaere et al. 2011).

Interestingly, these waves are subject to rapid damping while propagating along the coronal structures (Ofman & Wang 2002). This damping is primarily controlled by the thermal conduction, whereas the other dissipative mechanisms such as the viscosity and the radiation loss have a little role to play (De Moortel & Hood 2003). Furthermore, the wave damping is not uniform over the entire range of periodicities. In other words, the damping of slow waves has a frequency dependence. Krishna Prasad et al. (2012) showed that waves with shorter periods are restricted close to the base of the

coronal features, while those with longer periods propagate higher up. Gupta (2014) found two distinct height ranges (above the solar limb) with two contrasting damping rates. The frequency-dependent damping aspects in different coronal structures (on-disk fan loops and polar plumes/interplumes) have been explicitly shown using a single observation by Krishna Prasad et al. (2014). The authors have demonstrated that the frequency dependence of the damping observed in the on-disk loop like structures and the polar plume/interplume regions is different and neither of the observed dependences could be successfully explained by a linear MHD wave theory. However, using 3D MHD simulations, Mandal et al. (2016) showed that the observed characteristics for the on-disk loops are still consistent with the thermal-conduction-dominated damping of slow waves. Yet the peculiar frequency dependence found in the polar region structures remains unexplained. The earlier conclusions of Krishna Prasad et al. (2014) and Gupta (2014) were derived from isolated case studies based on a single data set, thus a statistical study is needed to establish the robustness of those results.

In this work, we revisit this anomalous damping behavior of the slow waves in polar regions by analyzing a large number of data sets. In the following sections, we describe the data and the analysis methods adopted, followed by the results and the conclusions.

2. Data

In this study, we used high-resolution EUV imaging data from the Atmospheric Imaging Assembly (AIA) (Lemen et al. 2012), on board *Solar Dynamics Observatory* (*SDO*) (Pesnell et al. 2012) from two different passbands, namely, AIA 171 Å and AIA 193 Å. We selected a total of 62 data sets, each covering about 180 minutes duration, taken over a span of seven years from 2010 to 2017. All of the data sets have a uniform cadence of 12 s with a spatial pixel scale ≈0″.6. As our

---

[3] Now at: Astrophysics Research Centre, School of Mathematics and Physics, Queen's University Belfast, Belfast BT7 1NN, UK.
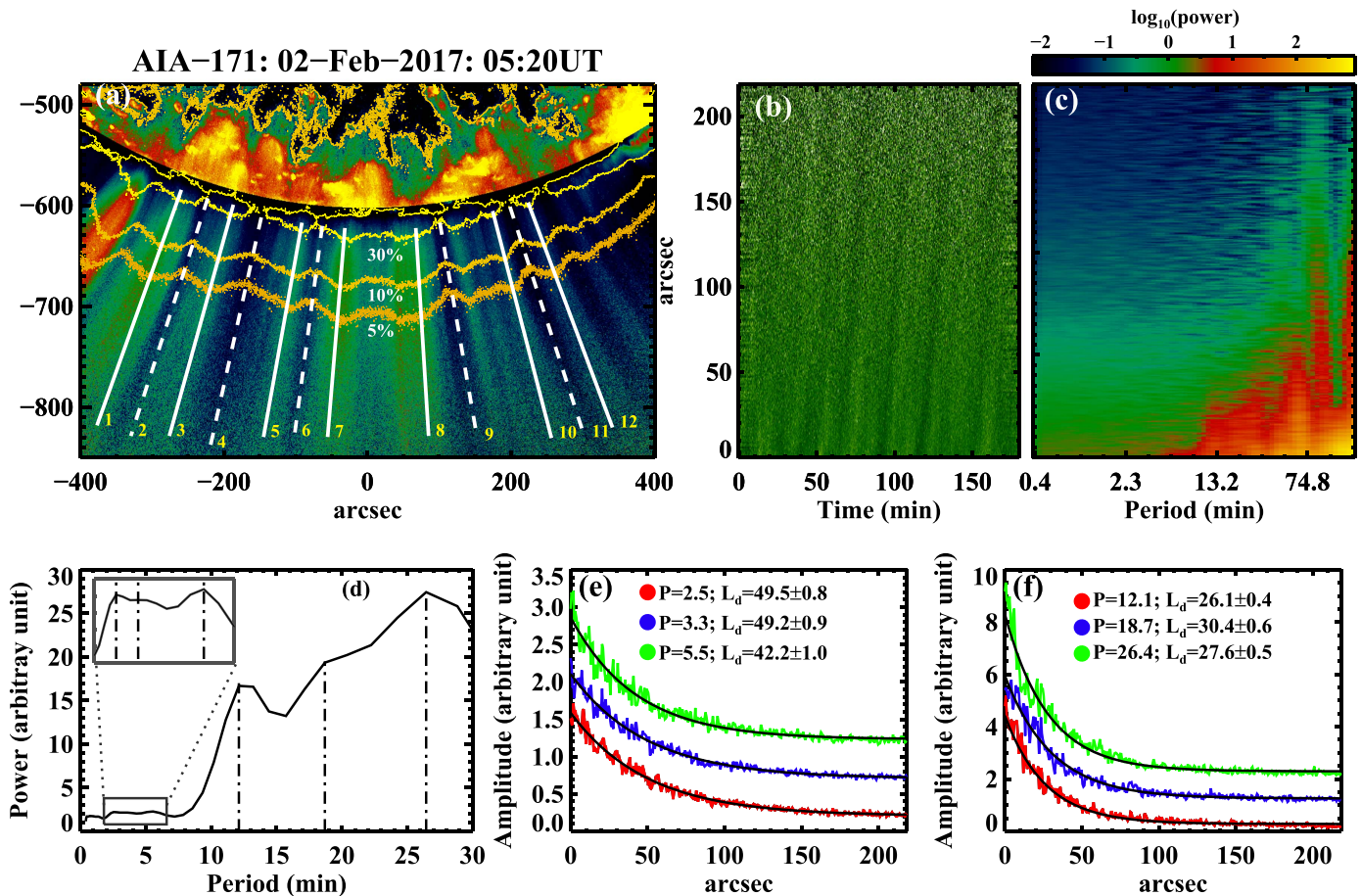
Figure 1. Methodology adopted to analyze the frequency-dependent damping in slow waves. Panel (a) shows a representative image of our ROI which has been processed using a radial filter to enhance the polar features. Overplotted yellow contours denote different intensity levels (as a percent of the on-disk intensity), obtained from the original image. Solid and dashed white lines represent the locations of the artificial slits used for generation of time–distance maps. An enhanced time–distance map, generated from slit 3, is shown in panel (b), whereas the corresponding period–distance map is shown in panel (c). Panel (d) displays a template power spectrum constructed from the period–distance map showing different periods present in the data. Panels (e)–(f) present the amplitude variation with distance for each of the detected periods. In these plots, the black solid lines show the fitted exponential decay function to the data. The obtained damping lengths (L_d) corresponding to individual periods (P) are printed on the panels.

primary targets are polar plume/interplume structures, all of the selected data are associated with coronal holes. Consequently, the sample do not contain any data sets observed between the end of 2012 and the end of 2014, i.e., during the maximum of current solar cycle (cycle 24). This also keeps our data free from large-scale background structures, such as streamers. Besides, all of the data sets were carefully checked with the JHelioviewer tool (Mueller et al. 2013) to exclude the possible presence of large- and small-scale jets, missing frames, etc., in the selected data.

3. Method

The full-disk data are first reduced to a smaller regions of interest (ROIs) of size $800'' \times 400''$ encompassing the polar region alone as shown in Figure 1(a). The bright plume and the dark interplume structures are then detected by following different intensity contour peaks and valleys (Krishna Prasad et al. 2011; Su 2014), respectively, as shown in the figure. The methodology adopted here to track the slow waves of different periods and study their damping, is similar to that described in Krishna Prasad et al. (2014) and Mandal et al. (2016). The overall procedure can be summarized as follows. First, we generate time–distance maps by extracting data from artificial

slits placed on top of the detected plume and interplume structures. The white solid and dashed lines marked on Figure 1(a) represent these slits for plume and interplume structures, respectively. The width of each of the slits is kept uniform and wide ($\approx 20''$) to improve the signal-to-noise ratio (S/N) in the generated time–distance maps. Figure 1(b) displays one such map obtained from slit 3, which has been further enhanced by subtracting (and then normalizing with) a background constructed from a running average of 300 frames (60 minutes) of the original data. Note that the bottom of the map corresponds to the limb. In this enhanced map, we readily identify the upwardly propagating slow waves as alternative slanted ridges. Such a classification of these intensity disturbances is primarily based upon the measurements of their (projected) phase speeds from the time–distance maps (Krishna Prasad et al. 2011; Mandal et al. 2015). A closer look at this map also reveals the simultaneous existence of multiple periods. This is particularly evident near the limb where we see many closely spaced ridges (shorter periods) as compared with a far away region where only sparsely spaced ridges (longer periods) are visible.

To isolate the power associated with the individual periods, we convert the original time–distance maps into period–distance maps (Figure 1(c)) by using a wavelet transformation
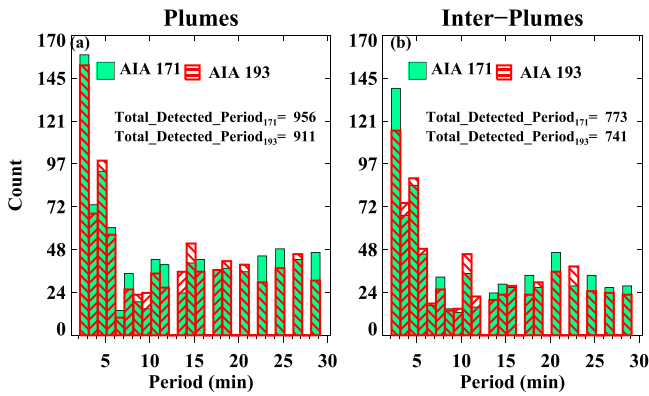
Figure 2. Distribution of the detected periods in plume (a) and interplume (b) regions. The results from the 171 Å and 193 Å passbands are shown in color-filled and cross-hatched blocks, respectively.

(Torrence & Compo 1998) of the timeseries at each spatial position. We note that the power at the longer periods is higher compared with that at the shorter periods and the power, at a given period, decreases as one moves away from the solar limb. A template power spectrum (Figure 1(d)) is constructed from the bottom 10 pixels of the period–distance map, which is used to identify the peak oscillation periods present in the data. For each detected period, the variation of the amplitude (defined as the square root of power) along the slit length is extracted as shown in Figures 1(e) and (f). Considering the cadence (12 s) and the duration (180 minutes) of individual data sets, we restrict our analysis to periods between 2 and 30 minutes. As can be seen, the oscillation amplitudes decrease rapidly with the distance. To measure the amplitude decay quantitatively, we fit the data with an exponential function (shown as solid black lines in the figure) defined as $A(x) = A_0 e^{-x/L_d} + C$, where L_d is the damping length. The L_d value obtained from the fit for each detected period is noted. In this way, we obtained damping lengths corresponding to multiple periods detected in several plume and interplume structures across all the 62 data sets in both 171 Å and 193 Å channels.

4. Analysis

4.1. Period Distribution

Figure 2 shows a histogram of all the detected periods in both plume and interplume structures observed in the two AIA passbands. The distribution is quite similar across different structures and passbands. The shorter periods (2–6 minutes) appear to be far more abundant than the longer periods (>7 minutes), which are more or less uniformly distributed. Although some previous studies Krishna Prasad et al. (2012) and Gupta (2014) reported the existence of both shorter and longer periods in the polar regions, it is generally believed that the long-period oscillations are more prevalent in these regions; therefore, this behavior is contradictory. Interestingly, upon careful inspection of the detected periods from individual data sets, we found that the same set of shorter periods are observed in several plume/interplume structures, whereas the longer periods observed in those structures are not necessarily the same. The latter are more or less evenly distributed across the period range between 7 and 30 minutes, producing such an imbalance. Overall, about 41% (43%) of the detected periods in 171 Å (193 Å) passband are from shorter (2–6 minutes) periods when the data from both plume and interplume structures are

combined. As the observed oscillations are mainly due to propagating waves (the periodicity of which is determined by the source), it is possible that the shorter- and the longer-period oscillations are generated from a different source. For instance, the short-period oscillations could be a direct result of leakage of global p-modes (De Pontieu et al. 2005; Calabro et al. 2013; Krishna Prasad et al. 2015), the chromospheric acoustic resonances (Botha et al. 2011), or the acoustic cutoff effect involving impulsive disturbances (Chae & Goode 2015), while the long-period oscillations are generated from transients (like spicules) in the lower atmosphere (Jiao et al. 2015; Samanta et al. 2015). These results must be taken into account when building a model (such as that of Yuan et al. 2016) to investigate the source of slow waves in polar regions.

4.2. Frequency Dependence

The obtained damping lengths, L_d, for all the detected periods, P (see Section 3), are shown in a log–log plot in Figure 3 separately for plumes and interplumes and in the two AIA channels. The gray points in these plots represent the actual values with the corresponding uncertainties. As one may notice, the damping-length values appear more scattered in the 193 Å passband as compared with that in the 171 Å passband. This is perhaps due to the S/N in the 193 Å passband. In fact, for a given passband, the scatter is relatively larger at longer periods. However, it is clear that the damping lengths become progressively shorter for longer periods. To quantitatively determine their dependence, we first construct a histogram of all the L_d values at a period bin and consider the damping length corresponding to the peak of that histogram as the representative L_d value at that period bin. Thus, obtained L_d values at each period bin are shown by black circles in Figure 3 (the errors are measured as the standard deviations of each distributions). These values are then fitted with a linear function (solid black line), the slope of which gives a measure of the dependence of damping length on the oscillation period. The obtained slope values are -0.3 ± 0.1, and -0.4 ± 0.1 for the plume and interplume structures, respectively, in the 171 Å passband. The corresponding values in the 193 Å passband are -0.3 ± 0.1 and -0.2 ± 0.1 for the plume and interplume structures. For comparison, the slopes obtained by Krishna Prasad et al. (2014) are -0.3 ± 0.1 and -0.4 ± 0.1 in the 171 Å and the 193 Å passbands, respectively. Note that Krishna Prasad et al. did not obtain separate values for plume and interplume structures due to limited statistics. Nevertheless, the fact that the slopes obtained from a large statistics in the present study are not very different from that reported by Krishna Prasad et al. from a single case study implies that the observed anomalous dependence of damping length on oscillation period is a general characteristic of slow waves in polar regions.

At this point, it is also intriguing to find out the range of the slope values by examining individual data sets. We therefore regroup the periods and corresponding damping lengths obtained from individual data sets and fit them separately to obtain respective slope values. Figure 4 displays the histograms of these values for plumes and interplumes. It appears the slope values in the 171 Å passband are narrowly distributed around -0.3 for plumes and skewed toward more negative values in interplumes. The corresponding values in the 193 Å passband show a relatively wider distribution, even with a few cases of positive (but close to zero) values. A majority of the cases still show negative slopes, but the peaks are shifted
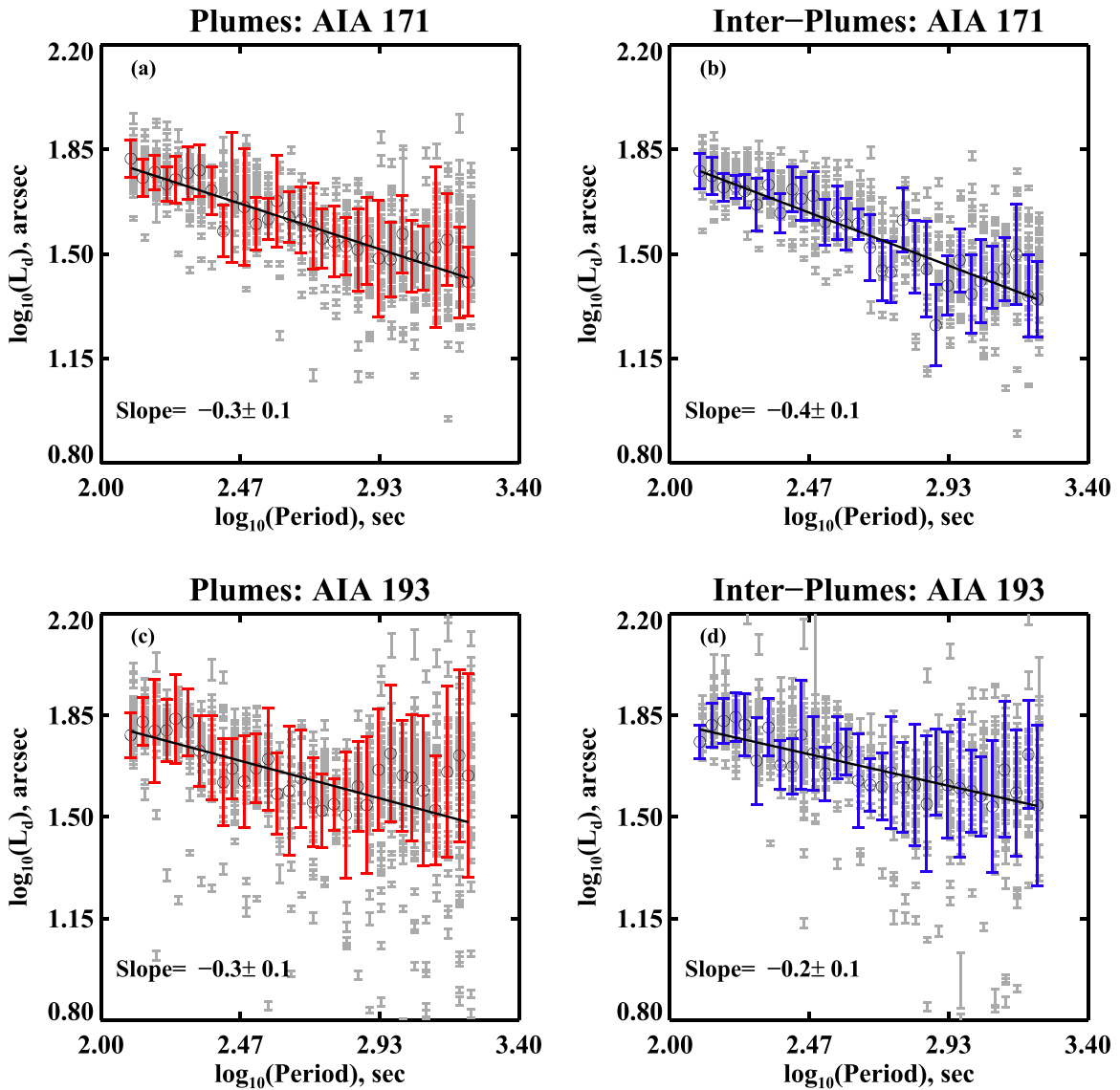
Figure 3. Damping length as a function of oscillation period in log–log scale. The top (bottom) panels display the results for the AIA 171 Å (193 Å) passband, while the left (right) panels show the results for plumes (interplumes). In each plot, the gray symbols represent the individual measurements whereas the black open circles denote the most frequent value for a given period. See the text for more details.

toward the less negative side compared with that in the 171 Å passband. To check the similarities between the distributions shown in Figure 4, we perform two nonparametric tests, namely Kolmogorov–Smirnov (K–S) test and the Mood test. The K–S test quantifies the distribution equivalence, whereas the Mood test checks for the equality of scale (Daniel 1990). All of these tests were performed using the statistical analysis software "R" (Feigelson & Babu 2012). Both the K–S test results (D_{plume} = 0.4, $D_{interplume}$ = 0.6 with $P < 0.001$) and the Mood test results ($P < 0.001$) indicate that the two distributions (panel (a) and panel (b) of Figure 4) are statistically different.

Let us now focus on the physical interpretation of the observed frequency dependence. The shorter damping lengths at the longer periods require the damping mechanism to be more efficient at low frequencies. Although there are several physical processes such as thermal conduction, compressive viscosity, radiation loss, gravitational stratification, magnetic field divergence, phase mixing, mode coupling etc. that could contribute to the damping of slow waves (De Moortel & Hood 2003, 2004; De Moortel et al. 2004), most of them are independent on frequency while a few (e.g., thermal conduction, compressive viscosity) are rather more efficient at high frequencies according to 1D linear MHD wave theory (see Table 1 in Krishna Prasad et al. 2014). One possible scenario is that a linear theory may not be a good scheme to describe slow waves in polar regions. In fact, Ofman et al. (2000) have used 1D and 2D MHD codes to study the nonlinear effects associated with slow-wave damping in the case of polar plumes and interplumes. These authors found that because of lesser plasma density, a stronger dissipation, in the nonlinear damping regime, is expected in the interplumes as compared to the plumes. However, from our observations (see Figure 3), we do not find any significant difference in damping-length values in these two regions. It is also interesting to note that the slope values too are not much different despite the plasma parameters like density, temperature, (and their gradients) being quite different in plumes and in surrounding interplumes (Wilhelm 2006; Wilhelm et al. 2011). Furthermore, the fundamental
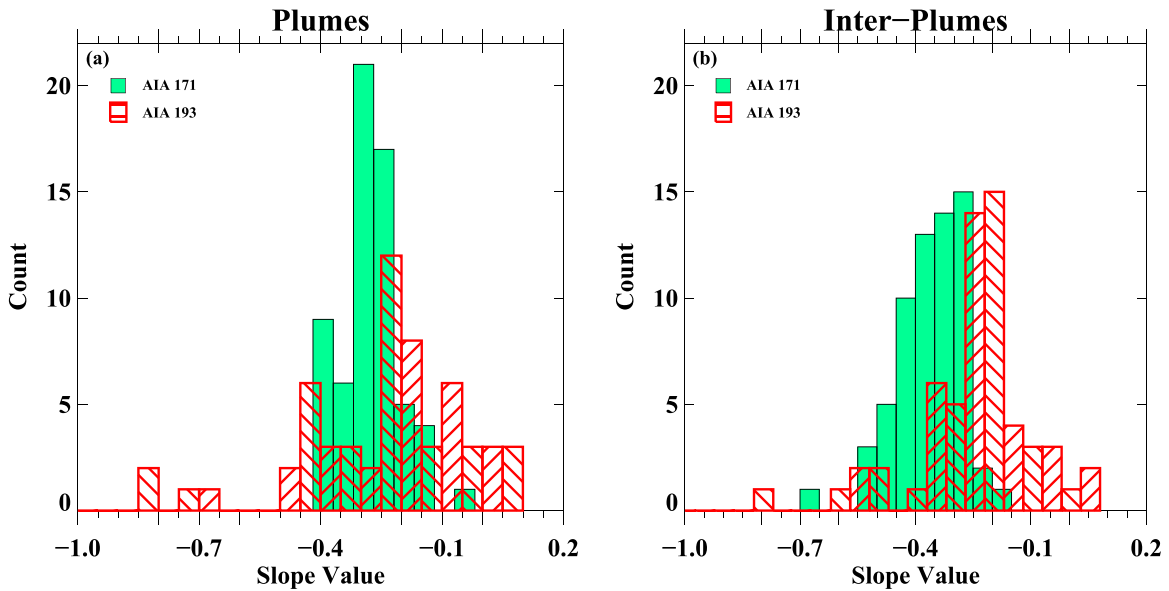
Figure 4. Distributions of the slope values obtained from damping-length–period relation similar to that derived in Figure 3, but from individual data sets.

mechanism through which the nonlinearly steepened slow waves are expected to dissipate is compressive viscosity, which is mainly effective at high frequencies. So it is not yet clear what mechanism causes this unusual frequency dependence in the damping of slow waves. Perhaps we need a full 3D description of slow waves to better understand their dissipation characteristics in polar regions.

4.3. Gaussian Decay of Amplitude

It has been shown that the amplitude of damping kink waves could be better described with a Gaussian profile rather than with the regularly used exponential profile (Pascoe et al. 2012, 2016). The strong damping observed in these waves is believed to be due to mode coupling (Pascoe et al. 2012; Hood et al. 2013), which is frequency dependent (Terradas et al. 2010). Although the equivalent theory and simulations are not yet available for slow waves, it is possible to check if the damping characteristics of slow waves show similar signatures. Indeed, Krishna Prasad et al. (2014) have shown (using a single example from a coronal loop) that for slow waves with longer periods, the amplitude decay is better approximated to a Gaussian function as compared with an exponential one. Using the large statistics available in this study, we explore this behavior by refitting the amplitude profiles (see Figure 1(e)) of all the detected periods with a Gaussian function (defined as $A(x) = A_0 \exp^{-x^2/L_d^2} + C$). We note the corresponding χ^2 values as a measure of goodness of fit and compare them with analogous values obtained from the exponential function defined in Section 3. It turns out that in only about 4% of the cases the Gaussian model fares better than the exponential model for the data from the 171 Å passband. This fraction is even less (<3%) for the data from the 193 Å passband. However, interestingly, the periodicities in all those cases were ⩾20 minutes. To check for the robustness of the above results, we also fit the damping curves using the maximum likelihood estimation (MLE) method and calculate the Akaike's An Information Criterion (AIC) to choose between the models (the smaller the AIC, the better the fit). We use the "mle" (includes "optim" also) procedure in R to compute the parameters.

Similar results were obtained confirming our finding that the amplitude decay in a very few cases (with periods ⩾20 minutes) appears to be a Gaussian-like rather than an exponential one.

In any case, at this point we are inclined to believe that an exponential decay model is good enough to describe the damping of slow waves.

4.4. The Power-law Index

In the previous sections, we discussed how the power at distinct peak periods decreases with distance as a consequence of the damping of slow waves and compared them to study the frequency dependence. However, it is also important to compare the relative levels of power at the full spectrum of frequencies with respect to each other particularly in the context of understanding MHD wave turbulence (Cranmer et al. 2015). One of the common ways to perform this is by fitting a power-law function (f^α) to the power spectra and noting the power-law index, α (Kolotkov et al. 2016; Battams et al. 2017). Such studies have been done in the past for different solar features: in chromospheric network and fibrils (Reardon et al. 2008); in active regions (Auchère et al. 2014); in polar plumes (Gupta 2014) in sunspot; moss; and quiet Sun (Ireland et al. 2015). In fact, Gupta (2014) studied the power-law behavior only at six locations in the polar region, and found that it resembles a Kolmogorov-turbulence-like behavior (Kolmogorov 1941). Utilizing the large database, in this study we derive the power-law indices from intensities at several plume, interplume structures corresponding to the two AIA passbands. A pixel location at about 30″ away from the solar limb (guided by our previously selected artificial slits) is chosen for each plume, interplume structure. To minimize the effect of noise, we perform an averaging during the power spectra generation processed, on a 5×5 pixel^2 area surrounding this location. In this case, this averaging is done in Fourier domain i.e., light curves from each of these pixels (within the mentioned 5×5 area) are subjected to Fourier analysis to get the corresponding power spectrum, and all these power spectra are then averaged to generate the final power spectra which is then fitted with a power-law function to get the power-law index. The locations closer to the limb are selected to get the
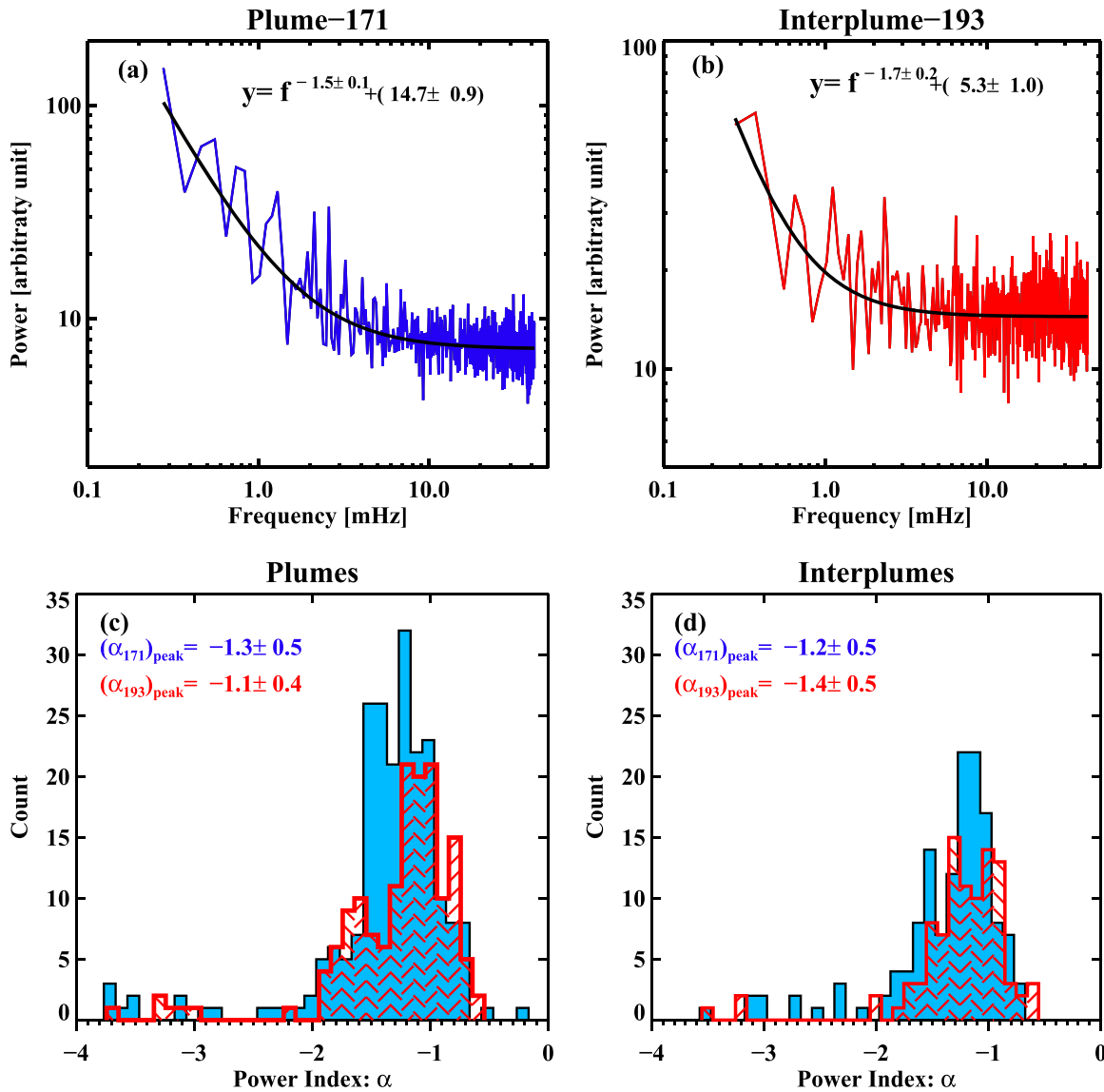
Figure 5. Panels (a)–(b) show two representative Fourier power spectra derived from the two AIA channels. The solid black curves represent the power-law fits, the indices of which are listed in the plot. The distributions of the power-law index (α) derived from all the data sets, are shown in panels (c)–(d) for different structures and passbands. Respective peak α values are printed on the panels.

power spectrum in full period range (Gupta 2014). While fitting the spectrum, we use statistical weights (i.e., $1/\sqrt{y}$) to minimize the effect of spurious power fluctuations around the higher frequencies. All of the spectra have been fitted with a function $Y = f^{-\alpha} + C$ where the constant term (C) represents the frequency-independent "white-noise" tail. Panels (a)–(b) of Figure 5 show two representative final Fourier power spectra (in log–log scale) obtained from a plume and an interplume structure. The overplotted black solid curves represent the fitted functions. The obtained α values are also listed in the plot. We fit the spectra only up to 0.27 mHz (60 minutes,) keeping in mind that the duration of every individual data set is 180 minutes. It may be noted that the α values derived in this way may have some influence from the chosen spatial binning of the data due to the autocorrelation and non-Gaussian noise.

We also constructed histograms of all the obtained α values to compare their distributions across different structures and passbands, which are shown in panels (c)–(d) of Figure 5. The

peak values from the respective data are listed in the plot. An immediate observation reveals that all these distributions (in different structures and passbands) are fairly similar, despite the different plasma parameters and magnetic field values in these regions. As we note, although our distributions have peaks around $\alpha \approx -1.2$, there are large number of occurrences close to $\alpha = -1.6$. Such an α value is probably a signature of the classical Kolmogorov-like ($\alpha = -5/3$) turbulence (Kolmogorov 1941). On the other hand, Jiao et al. (2016) showed that the peak at $\alpha \approx -1.2$ can also be interpreted as a signature of the underlying generation mechanism, which these authors attribute to the chromospheric spicules. The presence of both the scenarios as found in this study demands an in-depth study of the power-law index in these coronal structures (in fact, turbulence-driven coronal heating models show that turbulence can play a major role in dissipating the wave energies into the surrounding medium (Cranmer et al. 2007; Verdini et al. 2010)). Nonetheless, our study reveals a wider spectrum of α values as

opposed to the only Kolmogorov-like turbulence case as found by Gupta (2014).

5. Summary and Conclusions

We have performed a statistical analysis of the frequency-dependent damping of slow waves using high-resolution EUV imaging data. Previous case studies indicate anomalous behavior with longer wave periods damping faster than the shorter ones. In this study, we use a large sample of polar region data, to extract the exact frequency dependence, along with other useful properties. Below, we summarize the main results obtained from this study:

1. Intensity oscillations in polar regions are usually observed at longer periods. However, we find that the short-period (2–6 minutes) oscillations are at least as abundant as the long-period (>7 minutes) ones in both plume and interplume structures. The larger power available at the long-period oscillations makes them readily apparent suppressing the shorter periods.

2. The damping length and the oscillation period are weakly related through an inverse power-law function as previously found. The slope, as obtained by fitting the logarithmic values of these quantities, is -0.33 ± 0.05 for the plume and -0.38 ± 0.05 for the interplume structures, in the 171 Å passband. The corresponding values in the 193 Å passband are -0.28 ± 0.08 and -0.23 ± 0.07 for the plume and the interplume structures, respectively. The negative slopes could not be explained within the 1D linear MHD description of slow waves. Future theoretical and numerical studies with full 3D MHD are required.

3. A comparison of slopes obtained from individual data sets show that the values in the 193 Å passband are mostly negative but lower indicating a shallow dependence. On the other hand, the data from interplumes in the 171 Å passband show steeper dependence for a majority of the cases.

4. The decay of amplitude could be well described with an exponential function. A Gaussian profile was found to serve better only in about 4% of the cases, all of which correspond to longer periods (>20 minutes).

5. Finally, the Fourier power spectra near the limb show a power-law distribution with a peak close to $\alpha = -1.2$, suggesting a possible connection between the lower atmosphere transients with the generation of the observed coronal slow waves (Jiao et al. 2016). However, significant number of cases around $\alpha = -5/3$ perhaps indicate the physical nature of the underlying turbulence mechanism.

We hope these results will be useful to put some constraints on the numerical models of slow-wave propagation and dissipation. Also, further studies are required to explore more about the effects of turbulence on the damping of slow waves.

ORCID iDs

Sudip Mandal ⓘ https://orcid.org/0000-0002-7762-5629
S. Krishna Prasad ⓘ https://orcid.org/0000-0002-0735-4501
Dipankar Banerjee ⓘ https://orcid.org/0000-0003-4653-6823

References

Auchère, F., Bocchialini, K., Solomon, J., & Tison, E. 2014, A&A, 563, A8
Banerjee, D., Erdélyi, R., Oliver, R., & O'Shea, E. 2007, SoPh, 246, 3
Banerjee, D., & Krishna Prasad, S. 2016, GMS, 216, 419
Battams, K., Gallagher, B. M., & Weigel, R. S. 2017, arXiv:1707.02448
Botha, G. J. J., Arber, T. D., Nakariakov, V. M., & Zhugzhda, Y. D. 2011, ApJ, 728, 84
Calabro, B., McAteer, R. T. J., & Bloomfield, D. S. 2013, SoPh, 286, 405
Chae, J., & Goode, P. R. 2015, ApJ, 808, 118
Cranmer, S. R., Asgari-Targhi, M., Miralles, M. P., et al. 2015, RSPTA, 373, 20140148
Cranmer, S. R., van Ballegooijen, A. A., & Edgar, R. J. 2007, ApJS, 171, 520
Daniel, W. 1990, Applied Nonparametric Statistics (Boston, MA: Cengage Learning)
De Moortel, I., & Hood, A. W. 2003, A&A, 408, 755
De Moortel, I., & Hood, A. W. 2004, A&A, 415, 705
De Moortel, I., Hood, A. W., Gerrard, C. L., & Brooks, S. J. 2004, A&A, 425, 741
De Pontieu, B., Erdélyi, R., & De Moortel, I. 2005, ApJL, 624, L61
DeForest, C. E., & Gurman, J. B. 1998, ApJL, 501, L217
Feigelson, E., & Babu, G. 2012, Modern Statistical Methods for Astronomy: With R Applications (Cambridge: Cambridge Univ. Press)
Gupta, G. R. 2014, A&A, 568, A96
Hood, A. W., Ruderman, M., Pascoe, D. J., et al. 2013, A&A, 551, A39
Ireland, J., McAteer, R. T. J., & Inglis, A. R. 2015, ApJ, 798, 1
Jiao, F., Xia, L., Li, B., et al. 2015, ApJL, 809, L17
Jiao, F.-R., Xia, L.-D., Huang, Z.-H., et al. 2016, RAA, 16, 093
Kiddie, G., De Moortel, I., Del Zanna, G., McIntosh, S. W., & Whittaker, I. 2012, SoPh, 279, 427
King, D. B., Nakariakov, V. M., Deluca, E. E., Golub, L., & McClements, K. G. 2003, A&A, 404, L1
Kolmogorov, A. 1941, DoSSR, 30, 301
Kolotkov, D. Y., Anfinogentov, S. A., & Nakariakov, V. M. 2016, A&A, 592, A153
Krishna Prasad, S., Banerjee, D., & Gupta, G. R. 2011, A&A, 528, L4
Krishna Prasad, S., Banerjee, D., & Van Doorsselaere, T. 2014, ApJ, 789, 118
Krishna Prasad, S., Banerjee, D., Van Doorsselaere, T., & Singh, J. 2012, A&A, 546, A50
Krishna Prasad, S., Jess, D. B., & Khomenko, E. 2015, ApJL, 812, L15
Lemen, J. R., Title, A. M., Akin, D. J., et al. 2012, SoPh, 275, 17
Mandal, S., Magyar, N., Yuan, D., Van Doorsselaere, T., & Banerjee, D. 2016, ApJ, 820, 13
Mandal, S., Samanta, T., Banerjee, D., Krishna Prasad, S., & Teriaca, L. 2015, RAA, 15, 1832
Mueller, D., Dimitoglou, G., Caplins, B., et al. 2013, JHelioviewer: Visualization Software for Solar Physics Data, Astrophysics Source Code Library, ascl:1308.016
Ofman, L., Nakariakov, V. M., & Sehgal, N. 2000, ApJ, 533, 1071
Ofman, L., & Wang, T. 2002, ApJL, 580, L85
Pascoe, D. J., Goddard, C. R., Nisticò, G., Anfinogentov, S., & Nakariakov, V. M. 2016, A&A, 585, L6
Pascoe, D. J., Hood, A. W., de Moortel, I., & Wright, A. N. 2012, A&A, 539, A37
Pesnell, W. D., Thompson, B. J., & Chamberlin, P. C. 2012, SoPh, 275, 3
Poletto, G. 2015, LRSP, 12, 7
Reardon, K. P., Lepreti, F., Carbone, V., & Vecchio, A. 2008, ApJL, 683, L207
Roberts, B. 2000, SoPh, 193, 139
Samanta, T., Pant, V., & Banerjee, D. 2015, ApJL, 815, L16
Su, J. T. 2014, ApJ, 793, 117
Terradas, J., Goossens, M., & Verth, G. 2010, A&A, 524, A23
Torrence, C., & Compo, G. P. 1998, BAMS, 79, 61
Van Doorsselaere, T., Wardle, N., Del Zanna, G., et al. 2011, ApJL, 727, L32
Verdini, A., Velli, M., Matthaeus, W. H., Oughton, S., & Dmitruk, P. 2010, ApJL, 708, L116
Wilhelm, K. 2006, A&A, 455, 697
Wilhelm, K., Abbo, L., Auchère, F., et al. 2011, A&ARv, 19, 35
Yuan, D., Su, J., Jiao, F., & Walsh, R. W. 2016, ApJS, 224, 30